Unveiling the Outstanding Oxygen Mass Transport Properties of Mn-Rich Perovskites in Grain Boundary-Dominated La$_{0.8}$Sr$_{0.2}$(Mn$_{1−x}$Co$_x$)$_{0.85}$O$_{3±\delta}$ Nanostructures

Aruppukottai M. Saranya,[†] Alex Morata,[†] Dolors Pla,[†,‡] Mónica Burriel,[†,‡,§] Francesco Chiabrera,[†] Iñigo Garbayo,[†] Aitor Hornés,[†] John A. Kilner,[§,∥] and Albert Tarancón*,[†,⊥]

[†]Department of Advanced Materials for Energy Applications, Catalonia Institute for Energy Research (IREC), Jardins de les Dones de Negre 1, 08930 Sant Adrià del Besòs, Barcelona, Spain

[‡]CNRS, LMGP, Univ. Grenoble Alpes, F-38016 Grenoble, France

[§]Department of Materials, Imperial College London, London SW7 2AZ, U.K.

[∥]Electrochemical Energy Conversion Division, International Institute for Carbon-Neutral Energy Research (I2CNER), Motooka 744, Nishi-Ku, Fukuoka 819-0395, Japan

[⊥]ICREA, Passeig Lluís Companys 23, 08010 Barcelona, Spain

Ⓢ Supporting Information

ABSTRACT: Ion transport in solid-state devices is of great interest for current and future energy and information technologies. A superior enhancement of several orders of magnitude of the oxygen diffusivity has been recently reported for grain boundaries in lanthanum−strontium manganites. However, the significance and extent of this unique phenomenon are not yet established. Here, we fabricate a thin film continuous composition map of the La$_{0.8}$Sr$_{0.2}$(Mn$_{1−x}$Co$_x$)$_{0.85}$O$_{3±\delta}$ family revealing a substantial enhancement of the grain boundary oxygen mass transport properties for the entire range of compositions. Through isotope-exchange depth profiling coupled with secondary ion mass spectroscopy, we show that this excellent performance is not directly linked to the bulk of the material but to the intrinsic nature of the grain boundary. In particular, the great increase of the oxygen diffusion in Mn-rich compositions unveils an unprecedented catalytic performance in the field of mixed ionic−electronic conductors. These results present grain boundaries engineering as a novel strategy for designing highly performing materials for solid-state ionics-based devices.
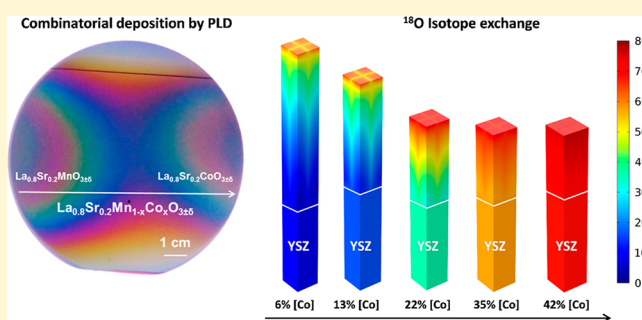
■ INTRODUCTION

Advanced energy conversion and storage devices, such as batteries, solar-to-fuel converters, fuel cells, and supercapacitors as well as novel solid-state electrochemical information storage and logic devices such as resistive switching memories are based on mixed ionic−electronic conductors (MIECs).[1] Recently, an intensive effort has been focused on looking for the enhancement of the ionic transport in MIECs.[2] Among other strategies, the implementation of nanoionics concepts based on engineering charge and mass transport properties at the nanoscale has been proposed to tune the functionality of interface-dominated structures like nanostructured or multilayered thin-film MIECs.[2] The search for enhanced ionic conductivity through the design of oxide interfaces has been pursued since Sata et al. showed superior anionic conductivity in the CaF$_2$/BaF$_2$ heterostructures due to space charge effects.[3] For oxygen ion conductors, multilayering epitaxial thin films have also been successfully proposed to tune the lattice strain, subsequently increasing the ionic

conductivity.[4] However, the implementation of this type of heterostructure still remains a challenge since it is limited to a certain number of substrates and to a demanding lateral architecture. Therefore, clear advantages would arise if this enhancement of mass and charge transport properties could occur at intrinsic material interfaces, such as grain boundaries (GBs).[5] This will open new technological perspectives for GB-dominated MIEC materials in advanced devices such as microsolid oxide fuel cells,[2,6,7] lithium ion batteries,[8,9] or nanoionics-based resistive switching devices.[10,11]

Recently, independent works from Navickas et al.,[12,13] Usiskin et al.,[15] and Tarancón and co-workers[14,16] have shown a great enhancement of the mass transport properties of nanostructures of La$_{0.8}$Sr$_{0.2}$MnO$_{3+\delta}$ (LSM). Several orders of magnitude of enhancement were reported for the oxygen mass

transport compared to the bulk properties in highly dense polycrystalline LSM thin films with vertically aligned grain boundaries. This enhancement was mostly attributed to the high concentration of strain-induced defects at the grain boundary level that even allowed the transformation of a mainly electronic conductor like LSM into a good mixed ionic electronic conductor comparable to the state-of-the-art $La_{0.8}Sr_{0.2}CoO_{3-\delta}$ (LSC). In this sense, grain boundary engineering can be considered a novel approach for substantially modifying the properties of oxygen ionic conductors and MIECs. However, a generalization of the enhancement of mass transport properties of MIEC oxides at the grain boundary level is far from being fully established. For instance, recent works by De Souza et al.[17,18] and Yildiz et al.[19,20] showed a deleterious effect on the ionic diffusivity with the presence of dislocations in the grain boundaries for $SrTiO_3$ and CeO_2. Therefore, to fully understand the oxygen diffusion enhancement in MIECs, further experimental and theoretical work is necessary to clarify and complement currently existing data. This will allow elucidating the origin of the phenomenon and controlling and tuning the mechanisms taking place in these materials.

To evaluate the scope of the grain boundary engineering approach, it is of particular interest to understand if the enhancement occurring in materials with low ionic conductivity is also happening in materials showing reasonably good mass transport properties at the bulk level. This can be rationally done by studying the effect of a high density of grain boundaries in the mass transport properties of a material system with tunable oxygen diffusivity and surface exchange. In this direction, it is well known that the substitution of Mn by Co in the $La_{0.8}Sr_{0.2}Mn_{1-x}Co_xO_{3\pm\delta}$ (LSMC) perovskite promotes significant changes in the oxygen mass transport properties, converting a mainly electronic conductor such as the oxygen hyperstoichiometric LSM into a reasonably good MIEC, like the oxygen-deficient perovskite LSC.[21,22]

In this work, we fabricate a thin film pseudobinary system $La_{0.8}Sr_{0.2}(Mn_{1-x}Co_x)_{0.85}O_{3\pm\delta}$ ($x \approx 0-1$) by using combinatorial pulsed laser deposition (C-PLD).[23-31] After proving the high quality of the films with fully dense and columnar-type nanostructures, required for accurate oxygen diffusion measurements, we show the evolution of the mass transport properties with cobalt content as directly measured by ^{18}O isotope exchange depth profiling coupled with time of flight secondary ion mass spectroscopy (IEDP-ToF-SIMS). Numerical simulations of the obtained diffusion profiles allow us to quantify the relevant bulk and grain boundary oxygen diffusion and surface exchange coefficients for different temperatures and cobalt contents. By comparing both sets of mass transport coefficients, we clearly prove an enhancement of grain boundary properties independently of the cobalt content. Finally, the electronic conduction properties of the LSMC family are measured, showing no direct correlation between the electronic properties and oxygen incorporation and therefore linking the origin of the enhanced properties to the enabling role of oxygen vacancies present at the grain boundary level.

■ EXPERIMENTAL SECTION

Small area, large area, and combinatorial depositions of LSM, LSC, yttria-stabilized zirconia YSZ (buffer layer), and LSMC thin film were performed by PLD. A PLD-5000 system from PVD products was used, coupled to a Lambda Physik COMPex PRO 205 KrF excimer laser (wavelength λ = 248 nm, pulse duration 20 ns, maximum power P = 30 W, and maximum repetition rate f = 50 Hz). Commercial targets with nominal compositions $La_{0.8}Sr_{0.2}MnO_3$ (LSM) and $La_{0.8}Sr_{0.2}CoO_3$ (LSC) (purity ≈99.95%, density ρ = 99.99%, diameter D = 2 in., and thickness t = 4 mm) from SurfaceNet GmBH Germany and homemade target 8 mol % Y_2O_3-stabilized ZrO_2 (8YSZ) (density ρ = 99.99%, diameter D = 4 in., and thickness t = 5 mm) were used as targets in PLD for thin film fabrication.

Structural X-ray diffraction (XRD) studies were performed using a Bruker D8 diffractometer equipped with Cu Kα radiation (λ = 1.54184 Å). The measurements were performed in the $\theta-2\theta$ (offset) scanning mode with step size 0.02°. The microstructures of LSM, LSC, YSZ, and LSMC thin films were studied by scanning electron microscopy (SEM) in a ZEISS AURIGA (equipped with energy-dispersive spectroscopy, EDS) microscope. The atomic percentage of the constituent elements in LSM, LSC thin films, and LSMC thin film system was studied by EDS and wavelength-dispersive spectroscopy (WDS, model Jeol JXA-8230) techniques.

Single crystal (100)-oriented 4 in. silicon wafers were employed as substrates for the oxygen exchange experiments. The Si/YSZ/LSMC heterostructures (see further details on the combinatorial sample deposition in the Supporting Information, section S.1) employed for the IEDP measurements were diced into 10×10 mm^2 by using an automatic dicing saw machine. Chemical cleaning of the sample surface was avoided to preserve, as much as possible, the surface from modification/contamination that could alter the surface exchange properties. A first thermal annealing at the selected exchange temperature in 200 mbar of dry pure (99.9996%) oxygen of normal isotopic abundance for at least 30 times the duration of the isotope exchange annealing was performed to equilibrate the oxygen stoichiometry of the PLD-deposited thin films. After this equilibration step, the sample was rapidly cooled, pure oxygen was evacuated from the chamber, and labeled oxygen was introduced instead. The isotope exchange was performed in 200 mbar of dry ^{18}O (55.3%) at the exchange temperatures (i.e., 600 and 700 °C for x = 0.6−0.8 and x < 0.6, respectively) for the selected time (1250−1500 s). Finally, the samples were quenched again to room temperature. The exchanged samples were analyzed by ToF-SIMS using a system from IONTOF (TOF.SIMS 5) equipped with a bismuth liquid metal ion source (LMIS) pulsed gun incident at 45°.

During the analysis, a 25 keV Bi$^+$ primary ion beam was used to generate the secondary ions via the low mass resolution or burst alignment mode (eight pulses) for analysis and a 2 keV Cs$^+$ beam incident at 45° for sputtering. The secondary ions were measured in the center of the sputtered crater in areas varying between 50×50 and 100×100 μm^2. The charge compensation during the analysis was solved by flooding low-energy electrons from the electron gun.

Electrical measurements were performed in a temperature-controlled Linkam probe station, after cutting the combinatorial sample in 1×0.5 cm^2 chips. Silver electrodes were used as contacts in 4-points in-plane electrical measurements (see details in Supporting Information, section S.5.1). The LSC parent compound thin film measured was deposited on a sapphire (0001) substrate to avoid crack formation and serve as a reference for the analysis.

■ RESULTS AND DISCUSSION

Continuous Compositional-Spread LSMC System. To study the dominating transport properties in nanostructured $La_{0.8}Sr_{0.2}(Mn_{1-x}Co_x)_{0.85}O_{3\pm\delta}$ (x = 0−0.8), a real continuous compositional-spread LSMC system was deposited in thin film form by combinatorial pulsed laser deposition (PLD). PLD is one of the methods of choice for preparing complex oxides thin films due to possible control of the stoichiometric transfer of the target composition and fully dense columnar-type nanostructures suitable for diffusion studies. The employed combinatorial PLD approach is based on the superposition of large-area films of the parent compounds, i.e., LSM and LSC, which follow a Gaussian shape (see sections S.2.1 and S.2.2 of
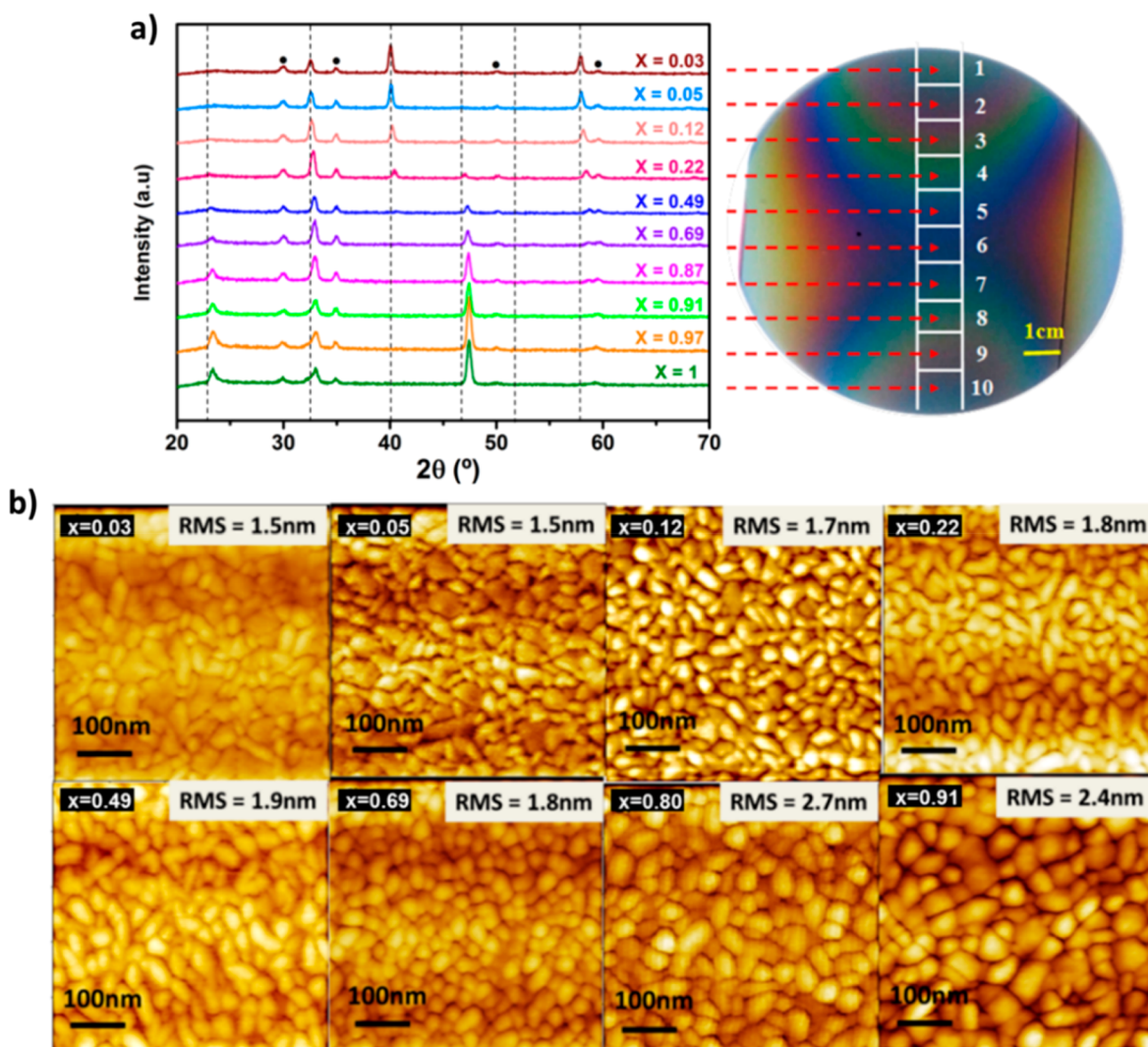
Figure 1. (a) XRD patterns of the LSMC system as a function of the Co content. The arrow marks indicate to which section of the combinatorial sample each XRD pattern corresponds. The vertical dashed lines corresponds to the position of the pseudocubic diffraction peaks of bulk LSM ($a_{pc,LSM}$ = 3.89 Å). (b) AFM images of the surface of the LSMC layer for different cobalt concentrations. The increasing evolution of the grain size and surface roughness was analyzed as a function of the Co content, obtaining values from 20 to 50 nm and from 1.5 to 2.7 nm, respectively.

the Supporting Information), centered at opposite sides of a 4 in. wafer substrate (further details on the superposition can be found in section S.2.3 of the Supporting Information). The different thickness of the LSM and LSC layers along the wafer defines the relative Co:Mn content, i.e., the composition of the final LSMC layer at each position. This *in situ* synthesis of the LSMC compound by interdiffusion of Mn and Co cations was achieved by depositing very thin (t_{max} = 1 nm) individual alternate LSM and LSC layers at high substrate temperatures (T = 700 °C, oxygen partial pressure of p = 2.66 Pa).[32−34] Under these conditions, the calculated effective interdiffusion time for Co and Mn is ∼1 s, ensuring instantaneous single phase formation. The final LSMC combinatorial sample covering the whole range of compositions ($La_{0.8}Sr_{0.2}(Mn_{1−x}Co_x)_{0.85}O_{3±δ}$; x ≈ 0−1) was grown on a 4 in. (100)-oriented Si wafer covered with a 100 nm thick yttria-stabilized zirconia (YSZ) layer. A reasonable thickness of the LSMC layer (from 80 to 175 nm) and a low Co-content gradient were defined to allow us obtaining a large spread of cobalt intermediate compositions with crack-free micro-structures.

A comprehensive structural and microstructural character-ization of the combinatorial sample was performed by various experimental techniques. The structural investigation was based on X-ray diffraction (XRD); the morphology was determined by scanning electron microscopy (SEM) and atomic force microscopy (AFM) of the surface, the thickness and composition distributions by SEM−energy dispersive spectroscopy (EDS) and wavelength dispersive spectroscopy (WDS), and the quality of the LSMC/YSZ interface by ToF-SIMS.

The series of XRD patterns acquired along the central axis of the LSMC combinatorial sample (corresponding to a predicted increment of the Co concentration from x = 0.03 to x = 0.94) show single phase deposition of polycrystalline YSZ and LSMC layers (Figure 1a). A shift of the perovskite peaks to higher angles was observed by increasing the Co doping concen-tration. This trend is in agreement with the shrinkage of the unit cell volume due to a continuous decrease of the lattice parameter as a function of the Co content from approximately a_{pc} = 3.90 to 3.84 Å (where a_{pc} refers to the pseudocubic lattice).[35−37] This decrease is generally ascribed to the smaller

average ionic radius of Co^{3+} (0.61 Å) compared to Mn^{3+} (0.645 Å) (Figure S13, section S.3.1). A change in peak intensity is observed when increasing the Co content (increase of the l00 reflections and decrease of the 111 and 211 reflections). This variation might be related to a preferential orientation appearing when increasing the Co content.

Cross-section and top-view SEM (Figures S14 and S15, section S.3.2) and AFM images (Figure 1b) demonstrate a full dense columnar-type microstructure with grain sizes in the nanoscale (20−50 nm) for the LSMC film. Low-magnification SEM surface images show crack formation for Co-rich compositions with $x > 0.8$ (Figure S15), limiting the current diffusion study to the range of compositions with $x < 0.8$. The series of AFM and SEM images confirms a morphological evolution with Co content with an increase in grain size from 20 to 50 nm (Figure S16, section S.3.3) and in surface roughness from 1.5 to 2.7 nm (Figure 1b).

The thickness distribution along the central axis of the LSMC combinatorial sample was studied by SEM (Figure 2a), showing good agreement with the thickness distribution predicted from the superposition of the two parent layers (details in sections S.2.2 and S.2.3 of the Supporting Information). Additionally, the composition distribution along the central axis of the combinatorial sample was studied by EDS and WDS. In Figure 2b, the atomic ratio of A- and B-site atoms of the LSMC system calculated from WDS is plotted against the wafer position. The atomic ratio of A-site cations (La and Sr) closely follows the nominal content of 80:20 for La:Sr. The atomic B-site ratio of Mn and Co cations follows a Gaussian distribution along the central axis (similarly to the thickness) showing a good agreement with the predicted values (Figure S17, section S.3.4). The atomic ratios between La/Sr (A-site), Mn/(Co+Mn) (B-site), and (La+Sr)/(Mn +Co) (A/B-site) atoms are also estimated from the atomic concentration, arising an average value of A/B ≈ 1.2, independent of the Mn/Co ratio or, in other words, of the position in the wafer. Interestingly, this indicates the presence of a B-site-deficient perovskite previously observed for low oxygen partial pressure PLD-deposited LSM layers.[38,39]

The quality of the multilayers was evaluated by ToF-SIMS. A typical SIMS depth profile of the different species contained in the LSMC/YSZ/Si system is presented in Figure S18, section S.3.5. The high quality of the multilayer is clearly visible by the sharpness of the interfaces, negligible interdiffusion between LSMC and YSZ, and the very small Si diffusion in the LSMC layer.

Oxygen Mass Transport Properties of the LSMC System. The oxygen transport in LSMC thin films was examined by mapping the combinatorial sample using IEDP-SIMS.[40,41] This is a direct method used to determine the oxygen kinetic parameters where oxygen mass transport takes place under zero electrochemical driving force.[42] The parameters acquired from IEDP-SIMS are typically the oxygen self-diffusion coefficient (D^*) and the oxygen surface exchange coefficient (k^*). To determine these oxygen transport parameters for the LSMC system, IEDP-SIMS experiments were performed at 600 and 700 °C. Silicon wafer substrates were employed to avoid oxygen diffusion intake from the backside during the exchange process, therefore limiting the incorporation of oxygen to the top surface area. The sputter time was converted into depth using thickness values of the films measured by SEM. The ^{18}O and ^{16}O secondary ions measured allowed calculating the ^{18}O isotopic fraction as a function of the distance to the top surface, $C'(x)$, corrected for the background isotope fraction (C'_{bckg}) and normalized to the ^{18}O concentration of the exchange gas (C'_g).

The obtained set of normalized isotopic fraction profiles for the whole range of compositions studied for 700 and 600 °C are presented in Figures 3a and 3b, respectively. Because similar exchange times (1250−1500 s) were employed for all experiments, higher isotopic concentrations and flatter diffusion profiles are roughly correlated to better oxygen mass transport properties. Accordingly, it is clear that increasing the cobalt content and temperature leads to an enhancement of the oxygen diffusion and exchange. At 700 °C the samples with high Co fractions above 0.6 were fully saturated in ^{18}O isotope; therefore, the samples corresponding to the Co-rich range (between $x = 0.6$ and 0.8) were analyzed at 600 °C. Note here that a dip in ^{18}O concentration was found near the surface for certain compositions, which can be related to back-exchange and/or slight cationic rearrangements near the surface (never affecting the data analysis presented here; see section S.4.2 for further details).

Similarly to previously reported by the authors for LSM thin films,[14] the shape of the oxygen diffusion profiles indicates that
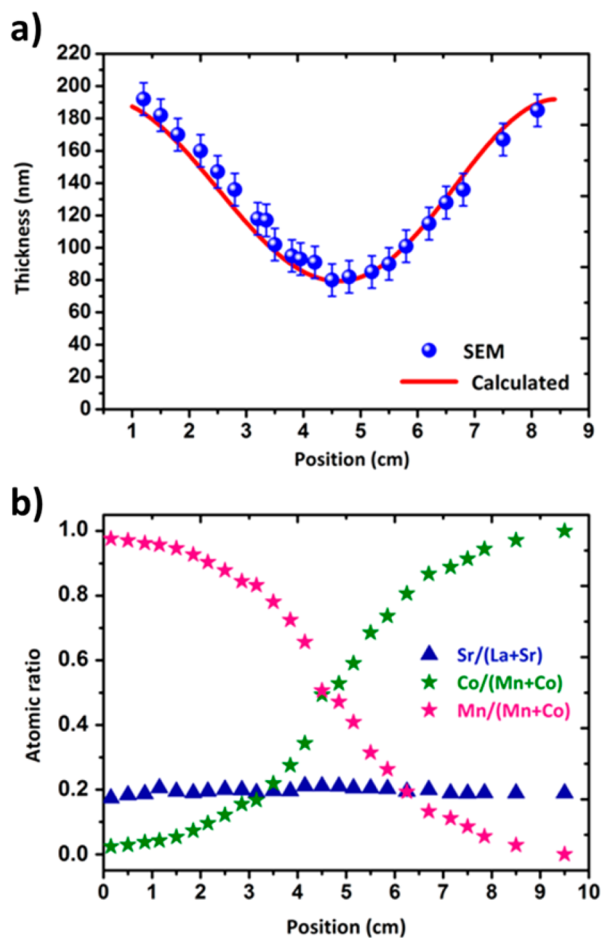

Figure 2. (a) Thickness and (b) composition along the central axis of the combinatorial sample obtained by SEM and WDS techniques, respectively. The calculated thickness in (a) refers to the superposition of the thickness profiles obtained for the individual parent compound layers, as shown in sections S.2.2 and S.2.3 of the Supporting Information. The Sr/(La+Sr), Co/(Mn+Co), and Mn/(Mn+Co) atomic ratio are included in (b).
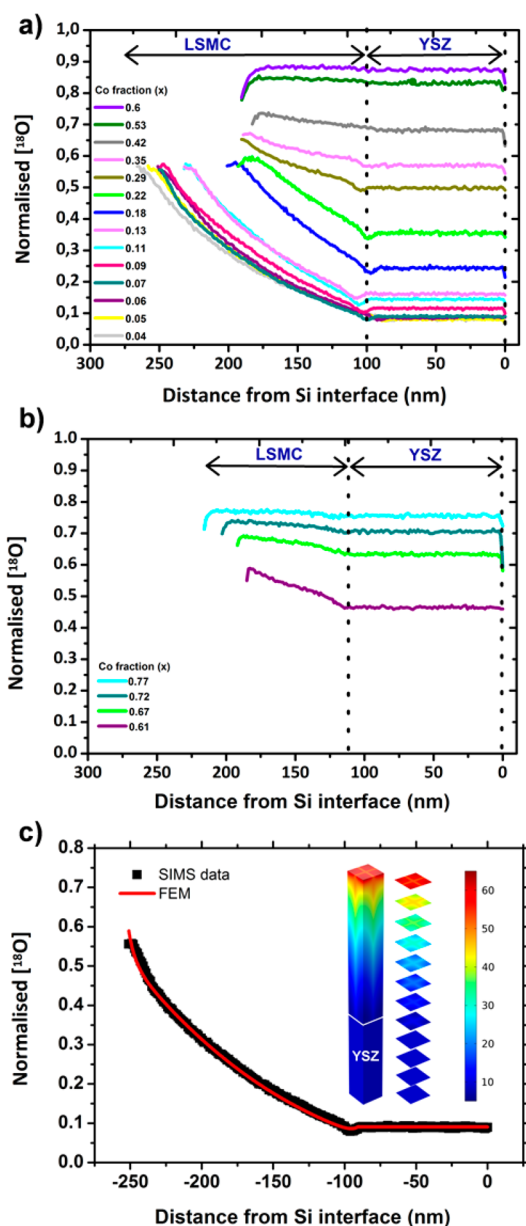
Figure 3. Normalized [18]O isotopic fraction depth profile obtained in LSMC/YSZ bilayers deposited on silicon substrates as obtained by IEDP-ToF-SIMS measurement. The *x*-axis represents the distance from the YSZ/Si interface. Isotope exchange temperatures of (a) 700 °C and (b) 600 °C are represented for different cobalt fractions. (c) Experimental and simulated oxygen isotope concentration profiles corresponding to the sample with 29% Co. The inset shows the cross-section 3D images of the oxygen isotope (^{18}O) concentration distribution map obtained by FEM for the same sample.

LSMC is not a homogeneous medium (the profiles present deep-penetrating diffusion tails and steps at the LSMC/YSZ interface). These profiles are fully compatible with the existence of narrow fast oxygen diffusion pathways across the LSMC film probably associated with grain boundaries of the columnar nanostructure generated by PLD. Because analytical solutions are not available for diffusion in such a heterogeneous bilayer thin film, the oxygen isotope diffusion profiles of the LSMC/YSZ bilayer were studied by the numerical finite element method (FEM) to extract the oxygen transport parameters along the bulk and grain boundaries of the LSMC

layer, i.e., D_b^*, D_{gb}^*, and k_b^*, k_{gb}^* (YSZ, $D^* = 3 \times 10^{-8}$ cm^2 s^{-1},[52] can be considered an oxygen sink in the range of temperatures and thicknesses under study). The geometry of the FEM model consists of a columnar cell made of four-half grains separated by 1 nm thick grain boundaries (see Figure S19, section S.4.1 for further details of the physical model). The average grain size values and thickness measured by SEM and AFM were used for the construction of the different geometries for the different compositions. Previously reported values of the bulk coefficients for the whole range of cobalt content[21,22] were employed as a starting point for the adjustment. For the grain boundary, manually adjusted values of diffusion and exchange coefficients (D_{gb}^* and k_{gb}^*) were used to simulate the experimental profiles. The shape of the experimental profiles was found to be very sensitive to D_b^*, D_{gb}^* and k_b^*, k_{gb}^* values, and they were adjusted until a good fit was obtained. As an example, the oxygen isotope profile simulated for a LSMC/YSZ bilayer with 6% Co ($x = 0.06$) is given in Figure 3c. The simulated profiles are in good agreement with the experimental profiles, confirming that the FEM model could fit the different regions of the experimental profile. The complete set of oxygen tracer diffusivities and surface exchange coefficients for bulk and GBs of the nanostructured LSMC was simulated and fitted. The 3D isotopic concentration maps generated by simulation after fitting the mass transport parameters clearly support the existence of an oxygen diffusion highway through the LSMC GBs from the top surface to the YSZ (see the inset in Figure 3c). It is interesting to mention that increasing the Co content makes the effect of the grain boundary less evident due to a homogenization of the isotopic concentration caused by an increase of the bulk diffusivity, which allows lateral diffusion from the GB into the bulk (Figure 4a).

Figures 4b and 4c show the set of oxygen mass transport coefficients obtained by FEM analysis as a function of the cobalt content and temperature. The values obtained for the bulk coefficients (D_b^* and k_b^*) are consistent with literature values[21,22] (also included in Figures 4b and 4c for comparison). On the other hand, for the whole range of cobalt under study, the GB coefficients are orders of magnitude larger than the bulk ones, indicating the presence of high diffusion pathways and excellent oxygen surface exchange. This enhancement represents a natural extension of the grain boundary effect previously observed for LSM to the LSMC family.[14,16]

Both grain boundary and bulk diffusivity increase with Co content (Figures 4b and 4c). The origin of the increase in the bulk diffusivity, more noticeable for $x > 0.2$, is due to the already reported increase of the oxygen vacancy ($V_O^{\cdot\cdot}$) concentration for the transition from an oxygen hyper-stoichiometric material (LSM) to a substoichiometric material (LSC).[24,36] Increasing the cobalt content shows a smaller effect on the GB diffusivity, probably due to the high concentration of oxygen vacancies present at the grain boundary level even before the B-site substitution with Co. This was previously suggested by Chiabrera et al.[16] after observing a negligible change of the ionic conductivity of nanostructured LSM when significantly decreasing the oxygen partial pressure.

Figure 4c shows an increase of the bulk surface exchange coefficient as a function of the cobalt content that is fully compatible with previously reported values in the literature.[21,22] Complementarily, a very large enhancement of the GB surface exchange coefficient is observed for the whole
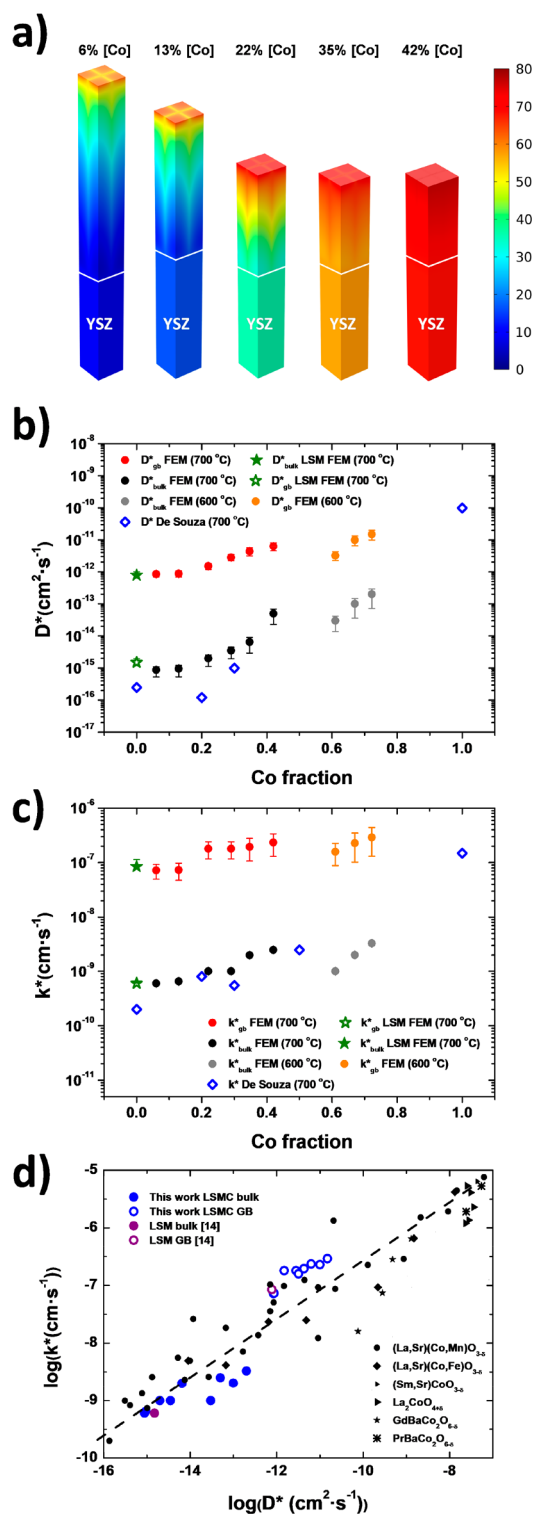
Figure 4. (a) Cross-section 3D images of the oxygen isotope (^{18}O) concentration distribution maps obtained by FEM for the whole range of Co content at $T = 700$ °C. (b) Oxygen self-exchange diffusion and (c) surface exchange coefficient along bulk and grain boundary extracted from simulation for $T = 600$ and 700 °C. The values are compared with bulk literature values[21,22] and with our previous work on LSM thin films.[15] (d) Correlation of the oxygen surface exchange coefficient $k*$ with the oxygen self-exchange diffusion coefficient $D*$ (literature values taken from De Souza et al.,[22] Saranya et al.,[14] and Tarancón et al.[43]).

range of Co content, suggesting that GBs control the oxygen incorporation in this type of interface-dominated LSMC materials. Importantly, k_{gb}^* happens to be roughly constant along the whole set of compositions and presents values eventually higher than those found in pure LSC for the entire LSMC family.

Despite the significant increase in mass transport properties of these GBs, the obtained results are still in good agreement with the empirical law, first proposed by Kilner and co-workers[22,44] which correlates $D*$ and $k*$ in a variety of MIEC perovskites. Figure 4d represents this correlation (log $D*$ vs log $k*$) for a set of perovskite materials with mixed ionic−electronic conduction reported in the literature, in comparison to the authors' results for interface-dominated LSMC and LSM layers. Notably, the superior properties of the GBs keep the trend reported for single phase perovskites despite the highly defective nature of these interfaces. This directly points out to a similar oxygen incorporation mechanism than the bulk material, although greatly enhanced by the high oxygen vacancy concentration at the grain boundary level.

Evolution of the Electrical Properties along the LSMC System. To gain further insights into the oxygen exchange variation with the Co content, we also analyzed the evolution of the in-plane electronic conductivity in the combinatorial sample as a function of the temperature. Figure 5a shows the evolution of the conductivity with the inverse temperature for the set of compositions. First, the adiabatic small polaron hopping model (see section S5 of the Supporting Information) could be fitted for the whole range of Co content, as reported for bulk samples.[35,45,46] The conductivity shows a minimum for intermediate composition ($x \sim 0.3$) and increases when approaching both parent compounds. Contrarily, the associated activation energies present a maximum at the same Co content ($x \sim 0.3$, see Figure 5b). In general, this critical point is linked, in solid solutions, to the activation of the conduction pathway through the dopant-cation sublattice for compositions above the percolation threshold, e.g., $x \sim 0.31$ in simple cubic lattices. This trend is also in good agreement with the existing literature for bulk LSMC, as presented in the same figure for direct comparison.[35] For bulk LSMC, the substitution of Mn by Co in La$_{1−x}$Sr$_x$MnO$_{3+\delta}$ progressively deteriorates the electrical conductivity because the difference in cations size and electronegativity generate lattice distortions and increase of carrier localization effects.[46,47] Similarly, Mn substitution of Co in pure LSC also reduces the electronic conduction due to the hole trapping effect of Mn cations.[48] Our films follow a similar trend of the activation energy presenting the maximum at $x \sim 0.3$, likely corresponding to the change in the electronic conduction from the Mn to the Co sublattice (also supported by the increase of the pre-exponential factor shown in Figure S24). However, our Mn-rich films have higher activation energies than the bulk. This might be related to chemical and structural defects present at the GB, which can lead to modifications of the Mn(Co)−O bonds and therefore to drastic changes of the electronic properties. The bulk behavior is fully recovered above the percolation threshold for Co-rich films.

This transition of the electronic conduction from the Mn- to Co-sublattice has however not a direct impact on the evolution of the surface exchange coefficient, suggesting that the electronic structure is not limiting the oxygen incorporation. In this direction, recent DFT studies[49] on LSM have shown that the availability of oxygen vacancies is controlling the
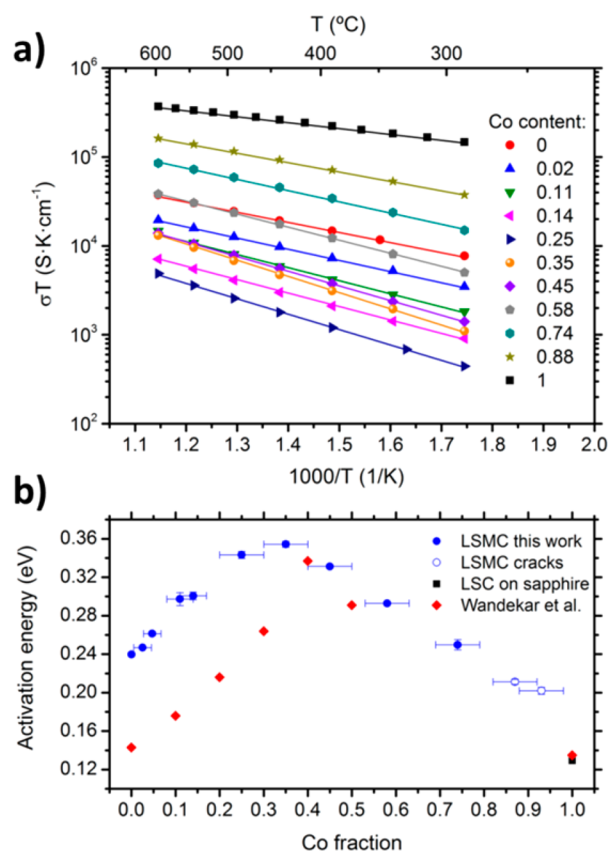
Figure 5. (a) In-plane electrical conductivity as a function of temperature for different Co content. (b) Activation energy derived from the conductivity measurements as a function of Co content. Lateral errors account for the predictable compositional variations in the LSMC films between the measuring electrodes. The open symbols refer to samples with visible cracks that could affect the conduction mechanism. The black squares with composition $x = 1$ refer to a LSC sample deposited on sapphire single crystal. Data from LSMC bulk sample from the literature are reported for comparison.[35]

surface exchange properties; moreover, Liu and co-workers showed that oxygen adsorption is highly favorable in LSM, eventually better than in LSC compounds.[50,51] Here, we experimentally unveil this theoretically predicted behavior linking it to the high availability of oxygen vacancies at the GB level, which completely change the bulk scenario in LSM for which the performance is limited by the extremely low concentration of oxygen vacancies. Under these conditions, the superior properties of GBs in Mn-rich LSMC compounds allow attaining high oxygen exchange coefficients comparable to those found in pure LSC.

All in all, high oxygen diffusion pathways along grain boundaries are found to be on the origin of the excellent mass transport properties presented here for the whole thin film LSMC family. Therefore, grain boundary engineering is presented as a new tool for overcoming a limited performance of bulk materials. This opens a new avenue for exploring new families of interface-dominated pure ionic or mixed ionic-electronic conductors for new applications.

CONCLUSIONS

A thin film pseudobinary system of $La_{0.8}Sr_{0.2}(Mn_{1-x}Co_x)_{0.85}O_{3\pm\delta}$ ($x \approx 0-1$) has been successfully deposited by combinatorial pulsed laser deposition to study the

oxygen mass transport properties at the bulk and grain boundary levels as a function of the cobalt content. Isotope exchange depth profiling coupled with SIMS measurement has been employed to obtain the oxygen self-diffusion (D_b^*, D_{gb}^*) and surface exchange (k_b^*, k_{gb}^*) coefficients for a large range of Co compositions at $T = 600-700$ °C ($x = 0-0.8$). While the bulk properties follow the behavior reported in the literature, this study reveals that grain boundaries act as fast diffusion and exchange pathways for oxygen ion transport dominating the transport properties of the whole material in the range of compositions under study. Moreover, supported by the electronic measurements performed on the whole LSMC family, the high oxygen exchange coefficients observed in Mn-rich compositions seem to be dominated by the high availability of oxygen vacancies, predicted by previous simulation studies. These results extend the striking enhancement, previously reported,[12,14,15] of mass transport properties in interface-dominated electronic conductors (LSM) to good ionic conductors (LSMC) and indicate that fast diffusion pathways found at the grain boundary level are not directly coupled to the bulk performance. The implications of these results are anticipated to be of great relevance for technologies that rely on mixed ionic–electronic conductor materials such as microsolid oxide fuel cells, lithium ion batteries, or nanoionics-based resistive switching devices, particularly if they are used in thin film form.

ASSOCIATED CONTENT

Supporting Information

The Supporting Information is available free of charge on the ACS Publications website at DOI: 10.1021/acs.chemmater.8b01771.

> Details of the experimental and computational methods; section S.1: deposition of combinatorial LSMC films by pulsed laser deposition; section S.2: optimization of the deposition of large-area parent compounds; section S.3: compositional and (micro)structural characterization of the combinatorial sample; section S.4: FEM simulations of the isotopic diffusion profiles of the LSMC/YSZ/Si system; section S.5: in-plane electrical characterization of LSMC sample (PDF)

AUTHOR INFORMATION

Corresponding Author

*(A.T.) E-mail: atarancon@irec.cat.

ORCID

Alex Morata: 0000-0002-3300-4636
Iñigo Garbayo: 0000-0003-2494-173X
Albert Tarancón: 0000-0002-1933-2406

Notes

The authors declare no competing financial interest.

support of the Juan de la Cierva postdoctoral program and A.M.S. of the FI predoctoral programmes (EU-European Social Fund).

■ REFERENCES

(1) Aricò, A. S.; Bruce, P.; Scrosati, B.; Tarascon, J.-M.; van Schalkwijk, W. Nanostructured Materials for Advanced Energy Conversion and Storage Devices. *Nat. Mater.* 2005, 4, 366−377.

(2) Maier, J. Nanoionics:Ion Transport and Electrochemical Storage in Confined Systems. *Nat. Mater.* 2005, 4, 805−815.

(3) Sata, N.; Eberman, K.; Eberl, K.; Maier, J. Mesoscopic Fast Ion Conduction in Nanometer-Scale Planar Heterostructures. *Nature* 2000, 408, 946−949.

(4) Kilner, J. Feel the Strain. *Nat. Mater.* 2008, 7, 838−839.

(5) Lin, Y.; Fang, S.; Su, D.; Brinkman, K. S.; Chen, F. Enhancing Grain Boundary Ionic Conductivity in Mixed Ionic-Electronic Conductors. *Nat. Commun.* 2015, 6, 1−9.

(6) Garbayo, I.; Pla, D.; Morata, A.; Fonseca, L.; Sabaté, N.; Tarancón, A. Full Ceramic Micro Solid Oxide Fuel Cells: Towards More Reliable MEMS Power Generators Operating at High Temperatures. *Energy Environ. Sci.* 2014, 7, 3617−3629.

(7) Tsuchiya, M.; Lai, B. K.; Ramanathan, S. Scalable Nanostructured Membranes for Solid-Oxide Fuel Cells. *Nat. Nanotechnol.* 2011, 6, 282−286.

(8) Moriwake, H.; Kuwabara, A.; Fisher, C. A. J.; Huang, R.; Hitosugi, T.; Ikuhara, Y. H.; Oki, H.; Ikuhara, Y. First-Principles Calculations of Lithium-Ion Migration at a Coherent Grain Boundary in a Cathode Material, LiCoO2. *Adv. Mater.* 2013, 25, 618−622.

(9) Rahman, M. M.; Wang, J. Z.; Hassan, M. F.; Wexler, D.; Liu, H. K. Amorphous Carbon Coated High Grain Boundary Density Dual Phase Li 4Ti 5O 12-TiO 2: A Nanocomposite Anode Material for Li-Ion Batteries. *Adv. Energy Mater.* 2011, 1, 212−220.

(10) Yang, J. J.; Pickett, M. D.; Li, X.; Ohlberg, D. A. A.; Stewart, D. R.; Williams, R. S. Memristive Switching Mechanism for Metal/oxide/metal Nanodevices. *Nat. Nanotechnol.* 2008, 3, 429−433.

(11) Waser, R.; Aono, M. Nanoionics-Based Resistive Switching Memories. *Nat. Mater.* 2007, 6, 833−840.

(12) Navickas, E.; Huber, T. M.; Chen, Y.; Hetaba, W.; Holzlechner, G.; Rupp, G.; Stöger-Pollach, M.; Friedbacher, G.; Hutter, H.; Yildiz, B.; et al. Fast Oxygen Exchange and Diffusion Kinetics of Grain Boundaries in Sr-Doped LaMnO 3 Thin Films. *Phys. Chem. Chem. Phys.* 2015, 17, 7659−7669.

(13) Navickas, E.; Chen, Y.; Lu, Q.; Wallisch, W.; Huber, T. M.; Bernardi, J.; Stöger-Pollach, M.; Friedbacher, G.; Hutter, H.; Yildiz, B.; et al. Dislocations Accelerate Oxygen Ion Diffusion in La 0.8 Sr 0.2 MnO 3 Epitaxial Thin Films. *ACS Nano* 2017, 11, 11475−11487.

(14) Saranya, A. M.; Pla, D.; Morata, A.; Cavallaro, A.; Canales-Vázquez, J.; Kilner, J. A.; Burriel, M.; Tarancón, A. Engineering Mixed Ionic Electronic Conduction in La 0.8 Sr 0.2 MnO 3+ δ Nanostructures through Fast Grain Boundary Oxygen Diffusivity. *Adv. Energy Mater.* 2015, 5, 1500377.

(15) Usiskin, R. E.; Maruyama, S.; Kucharczyk, C. J.; Takeuchi, I.; Haile, S. M. Probing the Reaction Pathway in (La0.8Sr0.2)-0.95MnO3+δ Using Libraries of Thin Film Microelectrodes. *J. Mater. Chem. A* 2015, 3, 19330−19345.

(16) Chiabrera, F.; Morata, A.; Pacios, M.; Tarancón, A. Insights into the Enhancement of Oxygen Mass Transport Properties of Strontium-Doped Lanthanum Manganite Interface-Dominated Thin Films. *Solid State Ionics* 2017, 299, 70−77.

(17) Waldow, S. P.; De Souza, R. A. Computational Study of Oxygen Diffusion along a [100] Dislocations in the Perovskite Oxide SrTiO 3. *ACS Appl. Mater. Interfaces* 2016, 8, 12246−12256.

(18) Metlenko, V.; Ramadan, A. H. H.; Gunkel, F.; Du, H.; Schraknepper, H.; Hoffmann-Eifert, S.; Dittmann, R.; Waser, R.; De Souza, R. A. Do Dislocations Act as Atomic Autobahns for Oxygen in the Perovskite Oxide SrTiO3. *Nanoscale* 2014, 6, 12864−12876.

(19) Marrocchelli, D.; Sun, L.; Yildiz, B. Dislocations in SrTiO3: Easy to Reduce but Not so Fast for Oxygen Transport. *J. Am. Chem. Soc.* 2015, 137, 4735−4748.

(20) Sun, L.; Marrocchelli, D.; Yildiz, B. Edge Dislocation Slows down Oxide Ion Diffusion in Doped CeO2 by Segregation of Charged Defects. *Nat. Commun.* 2015, 6, 6294.

(21) De Souza, R.; Kilner, J. A. Oxygen Transport in La1−xSrxMn1−yCoyO3±δ Perovskites Part I. Oxygen Tracer Diffusion. *Solid State Ionics* 1998, 106, 175−187.

(22) De Souza, R. A.; Kilner, J. A. Oxygen Transport in La1−xSrxMn1−yCoyO3±δ Perovskites: Part II. Oxygen Surface Exchange. *Solid State Ionics* 1999, 126, 153−161.

(23) Hornes, A.; Saranya, A. M.; Morata, A.; Tarancon, A. High-Throughput Screening of SOFC Cathode Materials. In *Proceedings of the 12th European SOFC & SOE forum*; 2016; p B1508.

(24) Thursfield, A.; Rossiny, J. C. H.; Fearn, S.; Kilner, J. A.; Metcalfe, I. S. A Combinatorial Approach to Synthesis of the La0.8Sr0.2Co1−yMnyO3±δ Family of Perovskite-Type Mixed Conducting Metal Oxides and Characterisation of the Surface Oxygen Mobility. *Solid State Ionics* 2012, 225, 182−185.

(25) Rossiny, J. C. H.; Julis, J.; Fearn, S.; Kilner, J. A.; Zhang, Y.; Chen, L.; Yang, S.; Evans, J. R. G. Combinatorial Characterisation of Mixed Conducting Perovskites. *Solid State Ionics* 2008, 179, 1085−1089.

(26) Christen, H. M.; Ohkubo, I.; Rouleau, C. M.; Jellison, G. E., Jr.; Puretzky, A. A.; Geohegan, D. B.; Lowndes, D. H. A Laser-Deposition Approach to Compositional-Spread Discovery of Materials on Conventional Sample Sizes. *Meas. Sci. Technol.* 2005, 16, 21−31.

(27) Christen, H. M.; Silliman, S. D.; Harshavardhan, K. S. Continuous Compositional-Spread Technique Based on Pulsed-Laser Deposition and Applied to the Growth of Epitaxial Films. *Rev. Sci. Instrum.* 2001, 72, 2673−2678.

(28) Fukumura, T.; Ohtani, M.; Kawasaki, M.; Okimoto, Y.; Kageyama, T.; Koida, T.; Hasegawa, T.; Tokura, Y.; Koinuma, H. Rapid Construction of a Phase Diagram of Doped Mott Insulators with a Composition-Spread Approach. *Appl. Phys. Lett.* 2000, 77, 3426−3428.

(29) Greer, J. A. History and Current Status of Commercial Pulsed Laser Deposition Equipment. *J. Phys. D: Appl. Phys.* 2014, 47, 034005.

(30) Christen, H. M.; Eres, G. Recent Advances in Pulsed-Laser Deposition of Complex Oxides. *J. Phys.: Condens. Matter* 2008, 20, 264005.

(31) Eason, R. *Pulsed Laser Deposition of Thin Films*; Eason, R., Ed.; John Wiley & Sons, Inc.: Hoboken, NJ, 2006.

(32) Noh, M.; Thiel, J.; Johnson, D. C. Synthesis of Crystalline Superlattices by Controlled Crystallization of Modulated Reactants. *Science (Washington, DC, U. S.)* 1995, 270, 1181−1184.

(33) Noh, M.; Johnson, C. D.; Hornbostel, M. D.; Thiel, J.; Johnson, D. C. Control of Reaction Pathway and the Nanostructure of Final Products through the Design of Modulated Elemental Reactants. *Chem. Mater.* 1996, 8, 1625−1635.

(34) Fister, L.; Johnson, D. C. Controlling Solid-State Reaction Mechanisms Using Diffusion Length in Ultrathin-Film Superlattice Composites. *J. Am. Chem. Soc.* 1992, 114, 4639−4644.

(35) Wandekar, R. V.; Wani, B. N.; Bharadwaj, S. R. Crystal Structure, Electrical Conductivity, Thermal Expansion and Compatibility Studies of Co-Substituted Lanthanum Strontium Manganite System. *Solid State Sci.* 2009, 11, 240−250.

(36) Petrov, A. N.; Voronin, V. I.; Norby, T.; Kofstad, P. Crystal Structure of the Mixed Oxides La0.7Sr0.3 Co1-Z MnzO3-Y (0 < z < 1). *J. Solid State Chem.* 1999, 143, 52−57.

(37) Troyanchuk, I. O.; Sazonov, A. P.; Szymczak, H.; Többens, D. M.; Gamari-Seale, H. Phase Separation in La2−xAx CoMnO 6 (A = Ca and Sr) Perovskites I. *J. Exp. Theor. Phys.* 2004, 99, 363−369.

(38) Li, Z.; Bosman, M.; Yang, Z.; Ren, P.; Wang, L.; Cao, L.; Yu, X.; Ke, C.; Breese, M. B. H.; Rusydi, A.; et al. Interface and Surface Cation Stoichiometry Modified by Oxygen Vacancies in Epitaxial Manganite Films. *Adv. Funct. Mater.* 2012, 22, 4312−4321.

(39) Chen, J.; Döbeli, M.; Stender, D.; Conder, K.; Wokaun, A.; Schneider, C. W.; Lippert, T. Plasma Interactions Determine the Composition in Pulsed Laser Deposited Thin Films. *Appl. Phys. Lett.* **2014**, *105*, 114104.

(40) Fischer, E.; Hertz, J. L. Measurability of the Diffusion and Surface Exchange Coefficients Using Isotope Exchange with Thin Film and Traditional Samples. *Solid State Ionics* **2012**, *218*, 18−24.

(41) Kilner, J. A.; Skinner, S. J.; Brongersma, H. H. The Isotope Exchange Depth Profiling (IEDP) Technique Using SIMS and LEIS. *J. Solid State Electrochem.* **2011**, *15*, 861−876.

(42) Crank, J. *The Mathematics of Diffusion*; Oxford Science: Oxford, UK, 1956.

(43) Tarancón, A.; Burriel, M.; Santiso, J.; Skinner, S. J.; Kilner, J. A. Advances in Layered Oxide Cathodes for Intermediate Temperature Solid Oxide Fuel Cells. *J. Mater. Chem.* **2010**, *20*, 3799−3813.

(44) Kilner, J. Isotopic Exchange in Mixed and Ionically Conducting Oxides. In *Proceedings of the Second International Symposium on Ionic and Mixed Conducting Ceramics*; Ramanarayanan, W. L., Worell, H. L., Tuller, H. L., Eds.; The Electrochemical Society Inc.: Pennington, NJ, 1994; pp 174−190.

(45) Ziese, M.; Srinitiwarawong, C. Polaronic Effects on the Resistivity of Manganite Thin Films. *Phys. Rev. B: Condens. Matter Mater. Phys.* **1998**, *58*, 11519−11525.

(46) Gayathri, N.; Raychaudhuri, A.; Tiwary, S.; Gundakaram, R.; Arulraj, A.; Rao, C. Electrical Transport, Magnetism, and Magneto-resistance in Ferromagnetic Oxides with Mixed Exchange Inter-actions: A Study of the La0.7Ca0.3Mn1-xCoxO3 System. *Phys. Rev. B: Condens. Matter Mater. Phys.* **1997**, *56*, 1345−1353.

(47) Bae, S.-Y.; Snyder, D. J.; Wang, S. X. Colossal Magneto-resistance in Sol-Gel Derived Epitaxial Thin Film of Co-Doped La1−xCaxMnOx. *J. Electron. Mater.* **1998**, *27*, 1−8.

(48) Kozhevnikov, V. L.; Leonidov, I. A.; Mitberg, E. B.; Patrakeev, M. V.; Petrov, A. N.; Poeppelmeier, K. R. Conductivity and Carrier Traps in La1-xSrxCo1-zMnzO3-δ(x = 0.3; z = 0 and 0.25). *J. Solid State Chem.* **2003**, *172*, 296−304.

(49) Mastrikov, Y. A.; Merkle, R.; Heifets, E.; Kotomin, E. A.; Maier, J. Pathways for Oxygen Incorporation in Mixed Conducting Perovskites: A DFT-Based Mechanistic Analysis for (La, Sr)-MnO3−δ. *J. Phys. Chem. C* **2010**, *114*, 3017−3027.

(50) Choi, Y.; Lin, M. C.; Liu, M. Rational Design of Novel Cathode Materials in Solid Oxide Fuel Cells Using First-Principles Simulations. *J. Power Sources* **2010**, *195*, 1441−1445.

(51) Choi, Y.; Lin, M. C.; Liu, M. Computational Study on the Catalytic Mechanism of Oxygen Reduction on La0.5Sr0.5MnO3 in Solid Oxide Fuel Cells. *Angew. Chem., Int. Ed.* **2007**, *46*, 7214−7219.

(52) Kilo, M.; Argirusis, C.; Borchardt, G.; Jackson, R. A. Oxygen diffusion in yttria stabilised zirconia—experimental results and molecular dynamics calculations. *Phys. Chem. Chem. Phys.* **2003**, *5*, 2219−2224.